CHEMISTRY OF MATERIALS

Communication

pubs.acs.org/cm

Valence Change Ability and Geometrical Occupation of Substitution Cations Determine the Pseudocapacitance of Spinel Ferrite XFe_2O_4 (X = Mn, Co, Ni, Fe)

Chao Wei,[†,⊥] Zhenxing Feng,[‡,⊥] Murat Baisariyev,[†] Linghui Yu,[†] Li Zeng,[¶] Tianpin Wu,[§] Haiyan Zhao,[∥] Yaqin Huang,[Δ] Michael J. Bedzyk,[¶,#] Thirumany Sritharan,[†] and Zhichuan J. Xu*[,†]

[†]School of Materials Science and Engineering, Nanyang Technological University, 50 Nanyang Avenue, Singapore 639798, Singapore

[‡]School of Chemical, Biological and Environmental Engineering, Oregon State University, Corvallis, Oregon 97331, United States

[¶]Graduate Program of Applied Physics, Northwestern University, Evanston, Illinois 60208, United States

[#]Materials Science and Engineering, Northwestern University, Evanston, Illinois 60208, United States

[§]X-ray Science Divisions, Argonne National Laboratory, Lemont, Illinois 60439, United States

[∥]Chemical and Materials Engineering Department, University of Idaho, Idaho Falls, Idaho 83401, United States

[Δ]College of Materials Science and Technology, Beijing University of Chemical Technology, Beijing 100029, People's Republic of China

Supporting Information

In recent years, spinel ferrites have attracted much attention as a merging material for oxygen reduction reaction (ORR),[1] advanced battery electrodes,[2,3] and supercapacitors.[4,5] Generally, the spinel structure can be described by a formula $[X_{1-\lambda}^{2+}B_{\lambda}^{3+}]^{T}[X_{\lambda}^{2+}B_{2-\lambda}^{3+}]^{O}O_4$, where λ is the inversion degree in-between 0 and 1, and superscripts T and O denote the tetrahedral and octahedral sites, respectively. Depending on the cation distribution, a spinel can be normal (λ = 0, 100% X in tetrahedral sites), inverse (λ = 1, 100% X in octahedral sites), or partially inverse ($0 < \lambda < 1$). Previous studies on spinel ferrites focused intensively on their magnetic properties,[6,7] as the substitution of Fe cations by transition metals can affect the cation distribution, thus resulting in significantly different magnetic properties due to the regulation of the unpaired electron spins of Fe^{2+} in octahedral sites.[8,9] Recent studies also showed that this substitution affects their electrochemical performance. For example, Mn substituted ferrites show nearly the same ORR activity as Pt/C in alkaline and Mn substitution also influences the capacitance more than other metal ion substituted ferrites.[1,10] Such difference on electrochemical performance could be ascribed to the type of substituent cations and their influence. However, no systematic mechanistic investigation has been carried out. This lack of knowledge hinders the understanding of the substitution effects on the performance and, thus, the development of spinel ferrites as energy materials.

In this communication, we report an investigation on the pseudocapacitive performance of spinel ferrites using an in situ X-ray absorption technique. As the pseudocapacitive behavior is associated with redox reactions of metal ions in the near-surface regions of oxides,[11,12] ferrite nanoparticles with diameters less than 10 nm were chosen to ensure the dominant contribution of the surface to X-ray absorption signals. In situ X-ray near edge structure (XANES) analysis was first conducted to screen the substitutions of Mn, Co, Ni, and Fe. The ability of the substitution cations to change their valence state within the spinel ferrite frame was found critical for offering pseudocapacitance. The rational was then given to the inversion degree, λ. The occupation of Mn cations in $MnFe_2O_4$ was further varied by heat treatment and investigated by extended X-ray absorption fine structure (EXAFS). The occupation of Mn cations was found influential in determining the pseudocapacitive performance of $MnFe_2O_4$.

XFe_2O_4 (X = Fe, Ni, Co, and Mn) nanoparticles were synthesized by a modified thermal decomposition method.[13] The electrodes were made by loading nanoparticles onto Vulcan carbon and the nickel foam was used as the current collector. Transmission electron microscopy (TEM) images (Figure 1a–d) show that these nanoparticles are well-dispersed on carbon and the size of nanoparticles is in the range of 7.0–9.5 nm (Figure S1). Synchrotron X-ray diffraction confirms their phase purity (Figure 1e). Figure 2a shows the representative cyclic voltammetry of these ferrites at a scan rate of 5 mV s^{-1} in 1 M Na_2SO_4. Clearly, $MnFe_2O_4$ has the largest capacitive area of all four ferrites. Figure 2b shows the specific capacitance of these ferrites normalized by particle mass and by specific surface area, respectively. The double layer capacitance contribution of Vulcan carbon (Figure S2) was subtracted according to the method we reported before.[14] The mass specific capacitance of $MnFe_2O_4$ is ~7 times higher than that of either Fe_3O_4 or $NiFe_2O_4$, and ~5 times higher than that of $CoFe_2O_4$. To exclude the surface area impact, the specific surface area of nanoparticles was measured by BET method and the capacitance of nanoparticles (after subtraction of carbon contribution) was normalized by their surface area to give the surface specific capacitance. Again, $MnFe_2O_4$ is remarkably higher than others. $CoFe_2O_4$ and $NiFe_2O_4$ show slight improvement in surface specific capacitance over Fe_3O_4.

Received: February 19, 2016
Revised: June 11, 2016
Published: June 13, 2016

DOI: 10.1021/acs.chemmater.6b00713
Chem. Mater. 2016, 28, 4129–4133

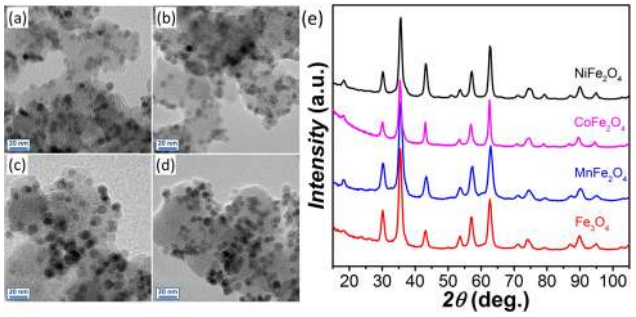

Figure 1. TEM images of carbon supported ferrite nanoparticles: (a) $MnFe_2O_4$, (b) $CoFe_2O_4$, (c) $NiFe_2O_4$, and (d) Fe_3O_4. Their average diameters are 7.0 ± 1.0, 8.1 ± 2.5, 9.5 ± 2.0, and 7.2 ± 0.9 nm, respectively. (e) Synchrotron X-ray diffraction patterns of these ferrites. The 2θ x-axis values are converted from 20 keV X-ray to Cu Kα X-ray.

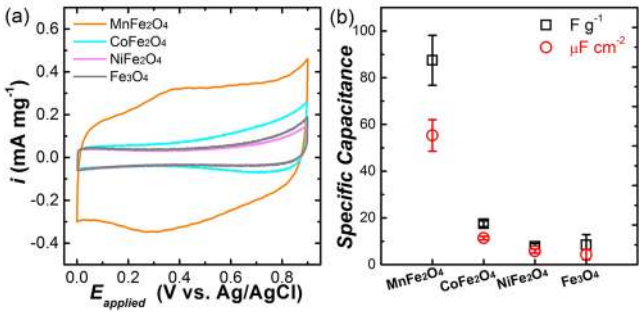

Figure 2. (a) Cyclic voltammetry of substituted ferrites in 1 M Na_2SO_4 at a scan rate of 5 mV s^{-1}. (b) Specific capacitance of ferrites based on mass of ferrites (black squares) and specific surface area of ferrite nanoparticles (red circles). The specific surface area of ferrite nanoparticles is obtained by BET method. The double layer capacitance contribution of Vulcan carbon has been subtracted.[14]

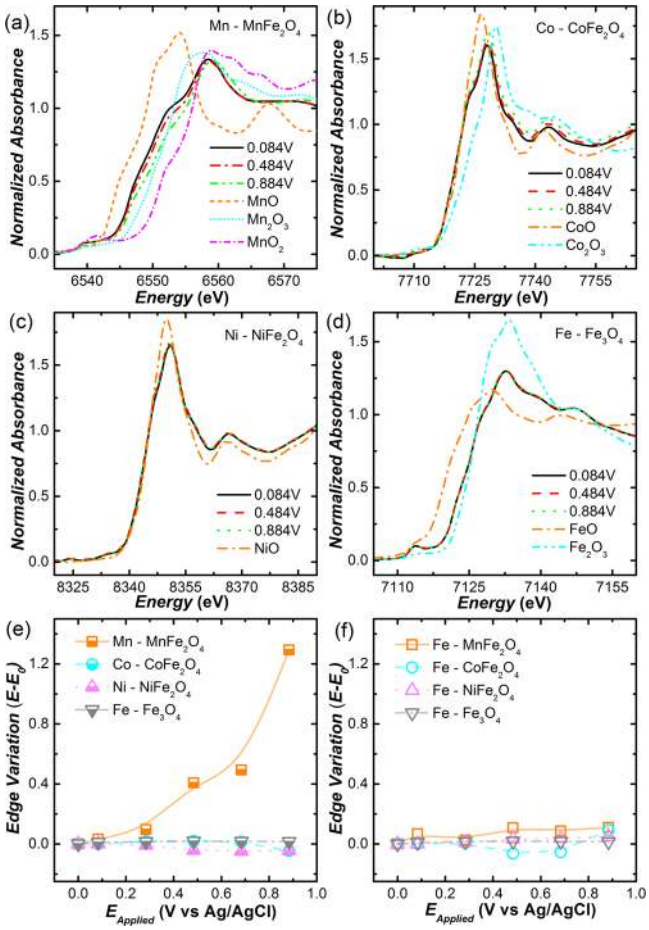

Figure 3. K-edge XANES spectra of Mn in $MnFe_2O_4$ (a), Co in $CoFe_2O_4$ (b), Ni in $NiFe_2O_4$ (c), and Fe in Fe_3O_4 (d) under various applied potentials. Applied potential induced K-edge shifts for substitution cations (e) and Fe (f). Detailed K-edge XANES spectra for all metals are shown in Figures S4 and S5.

These results indicate that the substitution of Mn in X of XFe_2O_4 increased the capacitance significantly.

To understand the underpinning mechanism, we performed in situ XAS measurements using a cell as shown in Figure S3. Because the contribution from the surface and near surface regions of the nanoparticles is dominant in our case, XAS can be employed to investigate the local chemistry changes of both Fe and the substitution cations X associated with the pseudocapacitive electrochemistry. Figure 3 shows K-edge XANES of these ferrites at applied potentials from 0 to 0.9 V vs Ag/AgCl. Clearly, only Mn exhibits significant edge shifts with the variation of potential. Figure 3a shows the Mn XANES of $MnFe_2O_4$ at the potential of 0.084, 0.484, and 0.884 V (the spectra collected at the potentials of 0, 0.284, and 0.684 V are in Figures S4 and S5). The standard powder samples of Mn^{2+} (MnO), Mn^{3+} (Mn_2O_3), and Mn^{4+} (MnO_2) were also measured for comparison. It can be seen that Mn XANES edge at 0.084 V lies between those of MnO and Mn_2O_3. To determine the Mn valence state, we used the integral method[15] to analyze the edge shift of X-ray absorption near edge structure (XANES), which is more accurate than the traditional inflation point method. Analysis (Figure S6) shows that the as-synthesized $MnFe_2O_4$ has Mn valence state of ~2.6+. This could be due to the heat treatment of $MnFe_2O_4$ in air, which oxidized some Mn^{2+} to Mn^{3+}.[16] Note that the analysis of Fe XANES gives the valence state of ~2.8+ (Figure S6), confirming the right stoichiometry of $MnFe_2O_4$. As the applied potential increased, the Mn XANES edge shifted gradually toward higher energy, indicating that the Mn valence state increased. As the potential reached 0.884 V, the edge shifted close to that of Mn_2O_3, indicating an oxidation state of ~2.9+ (Figure S6). The change in the Mn valence state is similarly observed for MnO_2 under the same potential windows, in which Mn cations in MnO_2 switches between 3+ and 4+.[12,17] Therefore, the lower capacitance of $MnFe_2O_4$ compared to MnO_2 may be partially attributed to the limited change of Mn oxidation state within the spinel frame. In addition, the high capacitance of MnO_2 is also due to its crystal features. For example, the channels among MnO_2 layers provide the space for accommodating charged species,[18] whereas there is no such a space in spinels. Interestingly, the valence state of Fe in $MnFe_2O_4$ did not change as the applied potential varied (Figure S6). We conclude that the pseudocapacitance of $MnFe_2O_4$ is predominantly contributed by the redox of Mn cations only, and not by Fe. This is different from the previous report that claimed Fe and Mn synergistically participated in the redox reactions, in which much larger particles were used as model materials.[19]

For $CoFe_2O_4$ and $NiFe_2O_4$, both Co and Ni remained their valence states at ~2+ (Figure 3b,c) within the applied potential window. Fe cations in these two ferrites also remained their valence state unchanged (Figure S4). Similarly, the Fe valence

DOI: 10.1021/acs.chemmater.6b00713
Chem. Mater. 2016, 28, 4129−4133

state of pure ferrite, Fe_3O_4, stayed the same (Figure 3d). For better comparison, Figure 3e,f shows the K-edge changes for Mn, Co, Ni, and Fe. It can be seen that only Mn exhibited a significant change in valence state, while all other metals remained unchanged. Note that the potential window employed in our tests covers the redox potential of some of these cations, e.g., Co^{2+}/Co^{3+} at ~1.1 V vs RHE and Co^{3+}/Co^{4+} at 1.4 V vs RHE.[20] However, the oxidation of Co cations relies on the high pH value (in KOH). At a neutral electrolyte (pH = 7), the oxidation of Co cations cannot be seen in the same potential window (1.5 V vs RHE).[21] This signifies that the low capacitance of other ferrites is mainly due to the lack of redox change within this potential window in our case. In addition, the specific capacitances per surface area of Fe_3O_4, $CoFe_2O_4$, and $NiFe_2O_4$ are within the electrical double layer capacitor range (<10 $\mu F/cm^2$) and therefore no pseudocapacitance occurs, which probably explains why no Fe, Co, Ni redox takes place as indicated by in situ XANES data.

Because MFO shows the highest capacitance among these spinel ferrites, extended X-ray absorption fine structure (EXAFS) analysis was performed to quantify further its atomic structure changes. There was negligible change in Fe EXAFS. However, significant increase of the Fourier transformed amplitude of Mn EXAFS was observed (Figure S7), particularly in the first shell region (1 Å < R < 2 Å). To quantify these atomic structure changes, detailed analysis of Mn and Fe EXAFS (Figure S8) as a function of applied potentials were performed and Table S1 lists these results. It is not surprising to see no change of Fe−O bond distances and coordination numbers, which is consistent with XANES measurements, and again suggests that Fe does not contribute to capacitance. Interestingly, the Mn−O bond distances remain the same, but an increase of the Mn−O coordination number is apparent as the applied potential is increased. It should be noticed that the coordination numbers for both Mn in octahedral and tetrahedral sites are lower than the standard numbers, i.e., 6 for Mn in octahedron and 4 for Mn in tetrahedron. This is because EXAFS signals are mainly from the surface region that has most under-coordinated cations, which is also postulated as one of origins for oxides' charge storage.[22] The coordination number increase is consistent with the valence state increase of Mn as observed by in situ XANES measurements, as higher oxidation states of Mn need more coordination to balance the charge. Attention was further given to the second shell region (2 Å < R < 4 Å) from in situ EXAFS (Figure S7), which shows negligible changes and suggests that the occupation of Mn remained unchanged. It further indicates that there is no occupation switch of Mn cations between the two geometry sites upon the applied potentials.

It is known that octahedral MnO_6 is the basic unit of MnO_2, in which the redox change between Mn^{3+} and Mn^{4+} is associated with its pseudocapacitance.[17] Recent studies also demonstrated that the octahedral MnO_6 unit is the active site of Mn-based perovskite oxides for oxygen electrocatalysis.[23−26] However, in spinel $MnFe_2O_4$, Mn cations can occupy both tetrahedral and octahedral sites, depending on the inversion degree λ. In particular, recent studies have shown that the site-occupation in spinel cobalt oxides can influence OER activity[27,28] and Mn substituted Co_3O_4 can improve capacitance.[29] To investigate further the influence of the Mn occupation, we varied the inversion degree by treating $MnFe_2O_4$ in air at 200, 300, and 400 °C for 6 h. The heat treatment can switch Mn cations from tetrahedral sites to octahedral sites and oxidize Mn^{2+} to Mn^{3+} at the same time.[9,30−32] Figure 4a shows the specific capacitance of heat-treated $MnFe_2O_4$ (their CVs are shown in Figure S9). The double layer capacitance contribution by Vulcan carbon has been subtracted to give the contribution of oxides only.[14] It can be seen that the $MnFe_2O_4$ capacitance increased with the increase of heat treatment temperature. In particular, the capacitance per surface area increased ~64% from 200 to 300 °C and ~192% from 200 to 400 °C. It should be noted that this increase is much higher than attributable to decrease of the specific surface area. The specific surface area decrease from 200 to 400 °C is only 23.7% (Figure S10) and the mass specific capacitance increased as well. Although this treatment can result in slight stoichiometry change, namely some excess oxygen, the spinel crystal structure is preserved (Figure S11) and the major consequence is Mn cation redistribution, which is reflected by the XANES prepeaks and EXAFS analysis. For 3d transition metal K edge XANES, the pre-edge peaks are assigned to the forbidden 1s→3d transition[33] and the change of the pre-edge peak intensity is indicative of the changes in the site occupation in tetrahedral and octahedral symmetry, namely narrower and more intense for the former and broader and less intense for the latter.[9,34,35] This is primarily because tetrahedral symmetry is highly noncentrosymmetric and this enables p→d transitions that contribute to the pre-edge peak.[36] When both tetrahedral and octahedral sites are occupied, the pre-edge peak will be the sum of these contributions, and the increase in intensity will be directly proportional to the tetrahedral site occupation.[36] As shown in Figure S12, the decrease of Mn K-edge prepeak intensities when annealing temperature goes up indicates more octahedral site occupations, whereas the

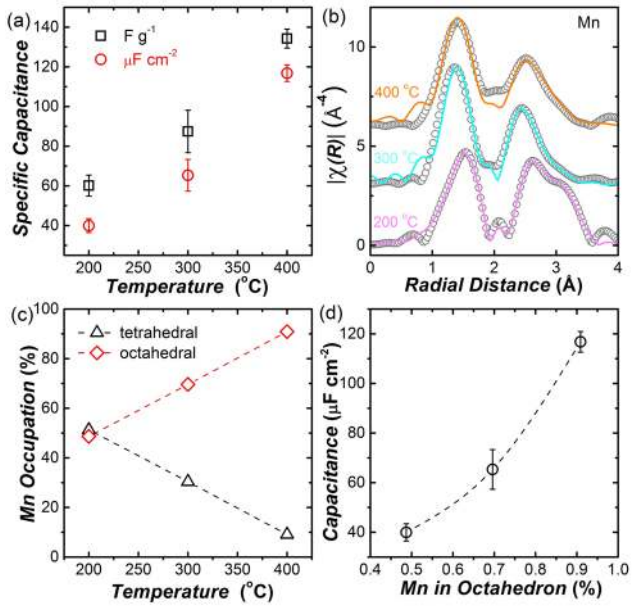

Figure 4. (a) Specific capacitance of $MnFe_2O_4$ heated treated in air at 200, 300, and 400 °C. Black squares and red circles refer to the capacitance based on the mass and the surface area of nanoparticles, respectively. The double layer capacitance contribution of Vulcan carbon has been subtracted.[14] (b) Fourier transforms (FT) of Mn K-edge EXAFS spectra of $MnFe_2O_4$. (c) Occupation of Mn cations in tetrahedral and octahedral sites as a function of temperature. (d) Specific capacitance per surface area of $MnFe_2O_4$ as a function of Mn in octahedral sites.

DOI: 10.1021/acs.chemmater.6b00713
Chem. Mater. 2016, 28, 4129−4133

increase of Fe K-edge prepeak intensities suggests more tetragonal site occupations after higher temperature annealing. Figure 4b and Figure S13 show Fourier transforms (FT) of Mn and Fe K-edge EXAFS spectra of $MnFe_2O_4$ treated at different temperatures. The remarkable differences of EXAFS indicate the different inversion degree of $MnFe_2O_4$. The significant difference in EXAFS spectra is also indicative of complicated changes after heating treatment (e.g., stoichiometry change and strong local disordering due to Mn redistribution). Figure 4c shows the occupation of Mn cations obtained by EXAFS analysis. For $MnFe_2O_4$ treated at 200 °C, ∼49% of Mn cations are in octahedral sites and ∼51% of them are in tetrahedral sites. For heat treatment at 300 °C, ∼70% of Mn cations are in octahedral sites and ∼30% of them stay in tetrahedral sites. Heat treatment at 400 °C further increased octahedral site occupation to ∼91% and very little amount in tetrahedral sites. The site occupation result is consistent with XANES observations and those reported previously.[31,32] Figure 4d shows the specific capacitance per surface as a function of the fraction of Mn in octahedral sites. The near-linear relationship suggests a strong correlation between the spinel capacitance and Mn site occupation. More Mn in octahedral sites leads to higher capacitance, indicating their dominant contribution.

In summary, we have investigated the pseudocapacitive behaviors of XFe_2O_4 (X = Mn, Fe, Co, and Ni) ferrite nanoparticles with diameters less than 10 nm. $MnFe_2O_4$ showed the highest specific capacitance among all the ferrites. The specific capacitance of $MnFe_2O_4$ is also the highest among reports to date due to its small particle size. To understand the mechanism that determines spinel capacitance, we performed detailed in situ XANES and EXAFS. We found that only Mn cations exhibited a significant valence state change. We attribute this change to the dominant contribution of the high pseudocapacitance in $MnFe_2O_4$. Co, Ni, and Fe remained with their valence states unchanged within the potential window, and therefore their capacitances are much lower than the Mn substituted ferrite. Fe cations in ferrites are stable and contribute nearly nothing to the pseudocapacitance. Analysis of in situ EXAFS shows that Mn cations simultaneously increased their oxygen coordination number to balance the Mn charge changes. The site occupation of Mn cations was further varied by heat treatment. We found that more Mn in octahedral sites resulted in higher capacitance. This is similar to MnO_2 and Mn-based perovskites, in which the octahedral MnO_6 unit is the active site. Although most Co (89%) and Ni (88%) locate at the octahedral site of $CoFe_2O_4$ and $NiFe_2O_4$ (Figures S15 and Table S4), the poor capability of changing valence state limits their capacitances. Therefore, we conclude that the ability of cation to change its oxidation state and its occupation of octahedral site (or the inversion degree) are influential in determining the spinel's pseudocapacitance. Our findings should be helpful to the prediction and the design of spinels for other electrochemical processes.

■ ASSOCIATED CONTENT

Supporting Information

The Supporting Information is available free of charge on the ACS Publications website at DOI: 10.1021/acs.chemmater.6b00713.

Materials synthesis, TEM analysis, XRD, XANES/EXAFS spectra and analysis of the ferrite nanoparticles (PDF).

■ AUTHOR INFORMATION

Corresponding Author

*E-mail: xuzc@ntu.edu.sg (Z. Xu).

Author Contributions

⊥These authors (Z. Feng, C. Wei) contributed equally.

Notes

The authors declare no competing financial interest.

■ ACKNOWLEDGMENTS

This work was supported by the Singapore Ministry of Education Tier 1 Grants (RGT13/13 and RG131/14) and the Singapore National Research Foundation under its Campus for Research Excellence And Technological Enterprise (CREATE) programme. LZ and MJB were supported by the MRSEC funded by NSF under DMR-1121262.The Advanced Photon Source (APS) at Argonne National Laboratory is supported by DOE under DE-AC02-06CH11357. Authors thank Charles Kurtz at APS 11ID and the APS 33BM beamline staffs.

■ REFERENCES

(1) Zhu, H.; Zhang, S.; Huang, Y.-X.; Wu, L.; Sun, S. Monodisperse $M_xFe_{3-x}O_4$ (M = Fe, Cu, Co, Mn) nanoparticles and their electrocatalysis for oxygen reduction reaction. *Nano Lett.* **2013**, *13*, 2947−2951.

(2) Feng, Z.; Chen, X.; Qiao, L.; Lipson, A. L.; Fister, T. T.; Zeng, L.; Kim, C.; Yi, T.; Sa, N.; Proffit, D. L.; Burrell, A. K.; Cabana, J.; Ingram, B. J.; Biegalski, M. D.; Bedzyk, M. J.; Fenter, P. Phase-controlled electrochemical activity of epitaxial Mg-spinel thin films. *ACS Appl. Mater. Interfaces* **2015**, *7*, 28438−28443.

(3) Ma, F.-X.; Hu, H.; Wu, H. B.; Xu, C.-Y.; Xu, Z.; Zhen, L.; Lou, X. W. Formation of uniform Fe_3O_4 hollow spheres organized by ultrathin nanosheets and their excellent lithium storage properties. *Adv. Mater.* **2015**, *27*, 4097−4101.

(4) Liu, S.; Sun, S.; You, X.-Z. Inorganic nanostructured materials for high performance electrochemical supercapacitors. *Nanoscale* **2014**, *6*, 2037−2045.

(5) Shi, W.; Zhu, J.; Sim, D. H.; Tay, Y. Y.; Lu, Z.; Zhang, X.; Sharma, Y.; Srinivasan, M.; Zhang, H.; Hng, H. H.; Yan, Q. Achieving high specific charge capacitances in Fe_3O_4/reduced graphene oxide nanocomposites. *J. Mater. Chem.* **2011**, *21*, 3422−3427.

(6) Wu, L.; Jubert, P.-O.; Berman, D.; Imaino, W.; Nelson, A.; Zhu, H.; Zhang, S.; Sun, S. Monolayer assembly of ferrimagnetic $Co_xFe_{3-x}O_4$ nanocubes for magnetic recording. *Nano Lett.* **2014**, *14*, 3395−3399.

(7) Fang, J.; Shama, N.; Tung, L. D.; Shin, E. Y.; O'Connor, C. J.; Stokes, K. L.; Caruntu, G.; Wiley, J. B.; Spinu, L.; Tang, J. Ultrafine $NiFe_2O_4$ powder fabricated from reverse microemulsion process. *J. Appl. Phys.* **2003**, *93*, 7483−7485.

(8) Sun, S.; Zeng, H.; Robinson, D. B.; Raoux, S.; Rice, P. M.; Wang, S. X.; Li, G. Monodisperse MFe_2O_4 (M = Fe, Co, Mn) nanoparticles. *J. Am. Chem. Soc.* **2004**, *126*, 273−279.

(9) Carta, D.; Casula, M. F.; Falqui, A.; Loche, D.; Mountjoy, G.; Sangregorio, C.; Corrias, A. A structural and magnetic investigation of the inversion degree in ferrite nanocrystals MFe_2O_4 (M = Mn, Co, Ni). *J. Phys. Chem. C* **2009**, *113*, 8606−8615.

(10) Kuo, S.-L.; Wu, N.-L. Electrochemical capacitor of $MnFe_2O_4$ with NaCl electrolyte. *Electrochem. Solid-State Lett.* **2005**, *8*, A495−A499.

(11) Lee, S. W.; Kim, J.; Chen, S.; Hammond, P. T.; Shao-Horn, Y. Carbon nanotube/manganese oxide ultrathin film electrodes for electrochemical capacitors. *ACS Nano* **2010**, *4*, 3889−3896.

(12) Toupin, M.; Brousse, T.; Bélanger, D. Charge storage mechanism of MnO_2 electrode used in aqueous electrochemical capacitor. *Chem. Mater.* **2004**, *16*, 3184−3190.

DOI: 10.1021/acs.chemmater.6b00713
Chem. Mater. 2016, 28, 4129−4133

(13) Xu, Z.; Shen, C.; Hou, Y.; Gao, H.; Sun, S. Oleylamine as both reducing agent and stabilizer in a facile synthesis of magnetite nanoparticles. *Chem. Mater.* **2009**, *21*, 1778−1780.
(14) Wei, C.; Lee, P. S.; Xu, Z. A comparison of carbon supports in MnO_2/C supercapacitors. *RSC Adv.* **2014**, *4*, 31416−31423.
(15) Dau, H.; Liebisch, P.; Haumann, M. X-ray absorption spectroscopy to analyze nuclear geometry and electronic structure of biological metal centers—potential and questions examined with special focus on the tetra-nuclear manganese complex of oxygenic photosynthesis. *Anal. Bioanal. Chem.* **2003**, *376*, 562−583.
(16) Zhang, Z. J.; Wang, Z. L.; Chakoumakos, B. C.; Yin, J. S. Temperature dependence of cation distribution and oxidation state in magnetic Mn−Fe ferrite nanocrystals. *J. Am. Chem. Soc.* **1998**, *120*, 1800−1804.
(17) Simon, P.; Gogotsi, Y. Materials for electrochemical capacitors. *Nat. Mater.* **2008**, *7*, 845−854.
(18) Devaraj, S.; Munichandraiah, N. Effect of crystallographic structure of MnO_2 on its electrochemical capacitance properties. *J. Phys. Chem. C* **2008**, *112*, 4406−4417.
(19) Kuo, S.-L.; Lee, J.-F.; Wu, N.-L. Study on pseudocapacitance mechanism of aqueous $MnFe_2O_4$ supercapacitor. *J. Electrochem. Soc.* **2007**, *154*, A34−A38.
(20) Han, B.; Qian, D.; Risch, M.; Chen, H.; Chi, M.; Meng, Y. S.; Shao-Horn, Y. Role of $LiCoO_2$ surface terminations in oxygen reduction and evolution kinetics. *J. Phys. Chem. Lett.* **2015**, *6*, 1357−1362.
(21) Bergmann, A.; Martinez-Moreno, E.; Teschner, D.; Chernev, P.; Gliech, M.; de Araujo, J. F.; Reier, T.; Dau, H.; Strasser, P. Reversible amorphization and the catalytically active state of crystalline Co_3O_4 during oxygen evolution. *Nat. Commun.* **2015**, *6*, 8625−8633.
(22) Wei, W.; Cui, X.; Chen, W.; Ivey, D. G. Manganese oxide-based materials as electrochemical supercapacitor electrodes. *Chem. Soc. Rev.* **2011**, *40*, 1697−1721.
(23) Stoerzinger, K. A.; Lü, W.; Li, C.; Ariando; Venkatesan, T.; Shao-Horn, Y. Highly active epitaxial $La_{(1-x)}Sr_xMnO_3$ surfaces for the oxygen reduction reaction: role of charge transfer. *J. Phys. Chem. Lett.* **2015**, *6*, 1435−1440.
(24) Stoerzinger, K. A.; Risch, M.; Han, B.; Shao-Horn, Y. Recent insights into manganese oxides in catalyzing oxygen reduction kinetics. *ACS Catal.* **2015**, *5*, 6021−6031.
(25) Suntivich, J.; Gasteiger, H. A.; Yabuuchi, N.; Nakanishi, H.; Goodenough, J. B.; Shao-Horn, Y. Design principles for oxygen-reduction activity on perovskite oxide catalysts for fuel cells and metal-air batteries. *Nat. Chem.* **2011**, *3*, 546−550.
(26) Suntivich, J.; May, K. J.; Gasteiger, H. A.; Goodenough, J. B.; Shao-Horn, Y. A perovskite oxide optimized for oxygen evolution catalysis from molecular orbital principles. *Science* **2011**, *334*, 1383−1385.
(27) Wang, H.-Y.; Hung, S.-F.; Chen, H.-Y.; Chan, T.-S.; Chen, H. M.; Liu, B. In operando identification of geometrical-site-dependent water oxidation activity of spinel Co_3O_4. *J. Am. Chem. Soc.* **2016**, *138*, 36−39.
(28) Kim, T. W.; Woo, M. A.; Regis, M.; Choi, K.-S. Electrochemical synthesis of spinel type $ZnCo_2O_4$ electrodes for use as oxygen evolution reaction catalysts. *J. Phys. Chem. Lett.* **2014**, *5*, 2370−2374.
(29) Perera, S. D.; Ding, X.; Bhargava, A.; Hovden, R.; Nelson, A.; Kourkoutis, L. F.; Robinson, R. D. Enhanced supercapacitor performance for equal Co−Mn stoichiometry in colloidal $Co_{3-x}Mn_xO_4$ nanoparticles, in additive-free electrodes. *Chem. Mater.* **2015**, *27*, 7861−7873.
(30) Vamvakidis, K.; Katsikini, M.; Sakellari, D.; Paloura, E. C.; Kalogirou, O.; Dendrinou-Samara, C. Reducing the inversion degree of $MnFe_2O_4$ nanoparticles through synthesis to enhance magnetization: evaluation of their 1H NMR relaxation and heating efficiency. *Dalton Trans.* **2014**, *43*, 12754−12765.
(31) Chen, J. P.; Sorensen, C. M.; Klabunde, K. J.; Hadjipanayis, G. C.; Devlin, E.; Kostikas, A. Size-dependent magnetic properties of $MnFe_2O_4$ fine particles synthesized by coprecipitation. *Phys. Rev. B: Condens. Matter Mater. Phys.* **1996**, *54*, 9288−9296.
(32) Gabal, M. A.; Ata-Allah, S. S. Concerning the cation distribution in $MnFe_2O_4$ synthesized through the thermal decomposition of oxalates. *J. Phys. Chem. Solids* **2004**, *65*, 995−1003.
(33) Shulman, G. R.; Yafet, Y.; Eisenberger, P.; Blumberg, W. E. Observations and interpretation of x-ray absorption edges in iron compounds and proteins. *Proc. Natl. Acad. Sci. U. S. A.* **1976**, *73*, 1384−1388.
(34) de Groot, F.; Vankó, G.; Glatzel, P. The 1s x-ray absorption pre-edge structures in transition metal oxides. *J. Phys.: Condens. Matter* **2009**, *21*, 104207−104213.
(35) Nilsen, M. H.; Nordhei, C.; Ramstad, A. L.; Nicholson, D. G.; Poliakoff, M.; Cabañas, A. XAS (XANES and EXAFS) investigations of nanoparticulate ferrites synthesized continuously in near critical and supercritical water. *J. Phys. Chem. C* **2007**, *111*, 6252−6262.
(36) Wilke, M.; Farges, F.; Petit, P.-E.; Brown, G. E.; Martin, F. Oxidation state and coordination of Fe in minerals: An Fe K-XANES spectroscopic study. *Am. Mineral.* **2001**, *86*, 714−730.

DOI: 10.1021/acs.chemmater.6b00713
Chem. Mater. 2016, 28, 4129−4133